Application of the Canonical Flexible Transition State Theory to CH_3, CF_3, and CCl_3 Recombination Reactions

Michèle Pesa, Michael J. Pilling,*,† and Struan H. Robertson

School of Chemistry, University of Leeds, Leeds, LS2 9JT, U.K.

David M. Wardlaw

Department of Chemistry, Queen's University, Kingston, Ontario K7L 3N6, Canada

Received: March 31, 1998; In Final Form: June 23, 1998

Canonical flexible transition state theory is applied to the recombination of CX_3 radicals (X = H, F, Cl) using a simple model for the potential-energy surface. The limiting high-pressure rate coefficient, k_∞, is calculated, using Monte Carlo integration with stratified sampling for the three reactions in the temperature range from 300 to 2000 K. k_∞ exhibits a negative temperature dependence, which becomes more pronounced as the size of X increases. There is a good agreement between the present results and some of the available experimental data. The factors that influence the negative temperature dependence of k_∞ and the relative magnitude of k_∞ for the three reactions are investigated.

I. Introduction

In the last few decades radical recombination reactions, which have no energy barrier along the reaction coordinate, have increasingly become the subject of theoretical and experimental studies. These reactions play an important role in combustion and atmospheric processes. Experimental measurements suggest that the temperature dependence of the limiting high-pressure rate coefficient, k_∞, can be negative for some reactions. Examples include the recombination of CCl_nH_{3-n} radicals, where the negative temperature dependence becomes steeper as n increases[1,2] and the recombination of t-C_4H_9 radicals.[3] The analysis of simpler radicals, e.g., $CH_3 + CH_3$ and $CH_3 + H$, which are more amenable to theoretical analysis, is more difficult because the reactions are in the falloff region so that k_∞ has to be determined by extrapolation and the comparatively subtle effects of temperature are more difficult to characterize. The temperature dependence of k_∞ is a matter of some controversy (see Figure 2 in ref 4). Radical recombination reactions, therefore, present an interesting challenge for theoreticians, the aim being to obtain a model which is physically transparent, is able to predict trends in the dependence of rate coefficients on temperature, on potential energy surface (PES) features, and on radical shape and size, and is also easy for the kinetics practitioner to use.

An early approach at trying to calculate the rate coefficient of associating radicals was the Gorin model,[5,6] which treated the system as a pair of fragments interacting via an isotropic central potential, the Hamiltonian of the internal modes being that of the isolated fragments. The dynamics of the interaction were governed solely by the central potential and the structure of the radicals was ignored. Benson[6] recognized that this was an oversimplification as there would be many encounters at short distances whose configurations would be repulsive. He attempted to correct for this by introducing the notion of a spherical surface centered at the bonding atom (with radius equal to the maximum collision parameter) divided into active and inactive regions. Reaction occurs only when the active regions of two such spheres touch each other. In this way, the structures of the associating radicals are approximately accounted for.

The statistical adiabatic channel model (SACM) of Quack and Troe,[7] in both canonical and microcanonical versions, provides a direct link to molecular and radical parameters (frequencies, rotational constants) but, at least in its early forms, accounted for their variation along the reaction coordinate parametrically. The first detailed analysis of the effects of the angular potential was provided by Wardlaw and Marcus[8] in their flexible transition state theory (FTST), a specific variant of variational transition state theory (VTST).[9] The model was further developed by Aubanel and Wardlaw,[10] Klippenstein and Marcus,[11] Klippenstein,[12] and Smith.[13] As in SACM, FTST divides the internal modes of motion into two types: *conserved* modes, i.e., those modes that do not change very much between reactants and products (typically vibrations), and *transitional* modes, which are large amplitude motions (modes which are vibrations in the parent molecule but become free rotors in the separated fragments). The advantage of FTST is that it incorporates a realistic representation of the transitional mode potential and accurately specifies the (classical) contribution of the transitional modes to the transition state (TS) sum of states. The disadvantage of including the full transitional mode potential into FTST is complexity of implementation, intensive numerical calculations, and reduced insight into the dependence of rate coefficients on PES features.

Therefore, efforts were made to develop a version of the original FTST which is easier to implement, involves less computation, provides more physical insight, and yet retains the essential features of FTST. In their investigation of the errors introduced in evaluating transitional mode properties classically rather than quantum mechanically, Klippenstein and Marcus[11] demonstrated that the integration over the conjugate momenta in the phase space integral defining the TS partition

† Present address: Molecular Simulations Ltd., 230/250 The Quorum, Barnwell Road, Cambridge, CB5 8RE, U.K.

10.1021/jp981700h CCC: $15.00
Published on Web 08/25/1998

function, which occurs in the expression for the canonical rate coefficient, could be done analytically, thereby greatly simplifying the overall integration procedure. Robertson et al. adopted a similar approach in their formulation of the canonical rate coefficient,[14] however, they used a body-fixed axis system in contrast to Klippenstein and Marcus who used a spaced-fixed system. The advantages of the body-fixed system are that the transitional potential is often defined in terms of internal coordinates such as bond lengths and angles, and so a minimal amount of transformation is required between coordinate systems; it also proved possible to analytically integrate more of the spatial coordinates than was previously possible. The model developed, canonical flexible transition state theory (CFTST), gives a simple expression for the high-pressure limiting thermal rate coefficient $k_\infty(T)$ when the reaction coordinate is defined as the distance between the centers of mass of the fragments. In this approach the contribution of the transitional modes to the rate coefficient is evaluated classically. The canonically derived rate coefficients are upper bounds to those obtained from microcanonical calculations, a consequence of the variational principle. Robertson et al.[14] used the $CH_3 + H \rightarrow CH_4$ recombination reaction to illustrate the validity and advantages of their version of the CFTST.

In this paper three related recombination reactions are investigated using CFTST:

$$CH_3 + CH_3 \rightarrow C_2H_6 \qquad \text{(R1)}$$

$$CF_3 + CF_3 \rightarrow C_2F_6 \qquad \text{(R2)}$$

$$CCl_3 + CCl_3 \rightarrow C_2Cl_6 \qquad \text{(R3)}$$

Reaction R1 is a benchmark. It was mainly chosen because of the availability of extensive experimental and theoretical data.[15−21] It also enables comparison of the results from this version of CFTST with the microcanonically and canonically derived rate coefficients for this recombination reaction by Wardlaw and Marcus.[4] For the analogous halogenated systems (R2 and R3) there is, despite their importance, a substantial uncertainty in the experimentally determined rate coefficients,[2,22−41] especially for reaction R2. The main aim of the paper is to model the temperature dependence of the rate coefficients for three recombination reactions which are anticipated to become more sterically hindered as the reactants become bulkier. Experimental data and FTST calculations for reaction R1 suggest a weak negative temperature dependence for this type of barrierless recombination reaction.

The structure of the paper is as follows: CFTST is reviewed briefly in section II, the potential-energy surface features are described in section III, and Results and Discussion are presented in section IV. The paper ends with Conclusions in section V.

II. Theory

II.1. Summary of CFTST. CFTST has been described previously in detail by Robertson, Wagner, and Wardlaw,[14] and only a brief summary follows. The high-pressure limiting canonical rate coefficient for association is given by

$$k_\infty(T) = g_e \frac{1}{\beta h} \frac{\sigma}{\sigma^\dagger} \frac{Q_{ts}(R^\dagger,T)}{Q_r(T)} e^{-\beta V(R^\dagger)} \qquad (1)$$

where g_e is the ratio of electronic degeneracies for the transition state (TS) and separated radicals, $\beta = 1/kT$, $\sigma/\sigma^\dagger$ is the ratio of reactant and transition state symmetry factors, $Q_r(T)$ is the total partition function for the reactants, $Q_{ts}(R^\dagger,T)$ is the TS partition function with the degree of freedom for the reaction coordinate removed, and $V(R)$ the potential energy along the reaction coordinate. The location $R^\dagger = R^\dagger(T)$ of the transition state is that value of the reaction coordinate at which k_∞ is minimized for a given temperature. The large amplitude transition state motion is included in $Q_{ts}(R,T)$. The division of internal modes into transitional and conserved modes allows the TS partition function to be written

$$Q_{ts}(R,T) = Q_c(R,T) Q_{tr}(R,T) \qquad (2)$$

Q_c, the partition function for the conserved modes, can be calculated within the harmonic oscillator approximation using standard harmonic oscillator partition functions. The dependence of the harmonic frequencies on the reaction coordinate is modeled by an exponential correlation between the separated radicals and the product molecule using a single correlation parameter α; details are provided in section III.2. The coupling between the transitional modes and external rotation as well as the inclusion of a realistic transitional-mode potential-energy function, V_{tr}, dictate that Q_{tr}, the partition function for the transitional modes, be evaluated using the classical partition function expression:

$$Q_{tr} = \frac{1}{h^n} \int \cdots \int e^{-\beta H} \, d\mathbf{p} \, d\mathbf{q} \qquad (3)$$

where H is the classical Hamiltonian for the transitional modes, n is the number of transitional/external rotation modes (excluding the reaction coordinate), $\mathbf{q}$ is the vector of the generalized coordinates, and $\mathbf{p}$ is the vector of their conjugate momenta. H can be written as the sum of a transitional mode kinetic energy T_{tr} and potential energy V_{tr}.

In specifying T_{tr} and V_{tr}, the fragments are assumed to be rigid bodies whose geometry depends on the reaction coordinate R but not on the five angles specifying the relative orientation of the principal axes of the two fragments. The R-dependence of the size and shape of the fragments is modeled using the same exponential correlation as that for the conserved mode frequencies; details are provided in section III.3. When separated from the full PES, V_{tr} can be expressed as a function of only these orientation angles and R.

The integral over the conjugate momenta in eq 3 can be performed analytically,[42] with the result

$$Q_{tr} = \left(\frac{2\pi}{\beta h^2}\right)^{n/2} \int \cdots \int |A|^{n/2} e^{-\beta V_{tr}} \, d\mathbf{q} \qquad (4)$$

where $|\boldsymbol{A}|$ is the determinant of the matrix whose coefficients A_{ij} appear in the expression for T_{tr}:

$$T_{tr} = \sum_{i,j=1}^{n} A_{ij} \dot{q}_i \dot{q}_j \qquad (5)$$

where the $\dot{q}_i$'s are generalized velocities. Robertson et al.[14] derived a specific expression for $|\boldsymbol{A}|$ when R, the progress along the reaction path, is the separation of the centers of mass of the

two fragments. Using this expression for $|\boldsymbol{A}|$, they showed that the rate coefficient is given by

$$k_\infty(T) = g_e \frac{1}{\beta h} \frac{\sigma}{\sigma^\dagger} \frac{e^{-\beta V^\dagger}}{Q_{\text{trans}}(T)} \left(\frac{Q_c^\dagger(T)}{Q_{\text{vib},1}(T) Q_{\text{vib},2}(T)} \right) \left(\frac{Q_{\text{pd}}^\dagger(T) Q_{\text{fr},1}^\dagger(T) Q_{\text{fr},2}^\dagger(T)}{Q_{\text{fr},1}(T) Q_{\text{fr},2}(T)} \right) \Gamma^\dagger(T) \quad (6)$$

where $Q_{\text{trans}} = (2\pi\mu kT)^{3/2}/h^3$ is the reduced mass translational partition function, $Q_{\text{vib},i}$ and $Q_{\text{fr},i}$ ($i = 1, 2$) are the vibrational and rotational partition functions of the fragments, $Q^\dagger_{\text{pd}} = 8\pi^2\mu(R^\dagger)^2 kT/h^2$ is a pseudo diatomic partition function for the relative orbital motion of fragments at the TS, and $Q^\dagger_c$, $Q^\dagger_{\text{fr},i}$ are the vibrational and rotational partition functions for the fragments at the TS. The configuration integral, Γ, is given by

$$\Gamma(R,T) \equiv (2^5\pi^3)^{-1} \int_0^\pi \mathrm{d}\theta_1 \sin\theta_1 \int_0^\pi \mathrm{d}\theta_2 \sin\theta_2 \int_0^{2\pi} \mathrm{d}\phi_1 \int_0^{2\pi} \mathrm{d}\phi_2 \int_0^{2\pi} \mathrm{d}\chi \, e^{-\beta V_{\text{tr}}} \quad (7)$$

where the angles θ_1, θ_2, ϕ_1, ϕ_2, and χ fully describe the relative orientation of the two (rigid) fragments. The angles are defined as follows: θ_1 and θ_2 are the angles between the C_3 axes and the vector between the centers of mass of the two fragments, ϕ_1 and ϕ_2 describe the rotation of the fragments about the C_3 axes, and χ is the dihedral angle of the C_3 axes. For a more detailed description of these angles, see also Figure 1 in ref 14. The form of the rate coefficient expression in eq 6 is especially appealing since the last three factors contain all the vibrational, shape (via moments of inertia), and transitional mode potential information, respectively. V_{tr}, which appears in the hindering function Γ, can be calculated from either a full ab initio potential or from a simple model. The transitional mode potential used in this work is described in detail in section III. It should be emphasized that the separation of the transitional mode partition function into various factors (Q_{pd}, $Q_{\text{fr},i}$, and Γ) derived by Robertson et al.[14] is exact within the classical framework and follows directly from the Aston and Eidinoff theorem[42]—no assumptions concerning the moments of inertia to be used in Q_{pd} or as to the nature of the top (e.g., near symmetric) are required. The model accounts for the change in transitional modes from vibrational through hindered rotor to free rotor seamlessly, incorporating the effects of anharmonicity in the transitional potential and the potential coupling between transitional modes. Also, no assumptions about the R dependence of the transitional mode partition function between the limits of reactants and products is assumed, a feature of many other treatments. (Note, in the section on the transitional potential below, analytic forms for certain features of transitional potential are assumed and the corresponding parameters are presented. This should not be confused with the common practice of assuming a functional form for the R dependence of the partition function and is indicative of the approximate nature of the potential used, not of the present treatment. The same approach could be used if a more accurate transitional mode potential was available.)

II.2. Monte Carlo Estimation of the Configuration Integral. The hindering function Γ consists of integrals over the relative orientation of the fragments and was evaluated using a Monte Carlo (MC) algorithm. Monte Carlo techniques are discussed extensively elsewhere,[43] and so only a brief discussion will be given here. In the simple Monte Carlo integration of a function f over a volume V, random points are sampled uniformly from V, the integral being estimated as

$$\int_V f \, \mathrm{d}V \approx V\langle f \rangle \pm V \sqrt{\frac{\langle f^2 \rangle - \langle f \rangle^2}{N}} \quad (8)$$

where

$$\langle f \rangle \equiv \frac{1}{N} \sum_{i=1}^{N} f_i$$

and

$$\langle f^2 \rangle \equiv \frac{1}{N} \sum_{i=1}^{N} f_i^2 \quad (9)$$

and the last term of eq 8 represents the 1σ confidence interval. In the present case, $f = \Gamma \times (2^5\pi^3)$. For the current systems, this method is very computer intensive, since many regions of the volume contribute little to the integral and so many MC points are needed to keep the variance low. This situation is exacerbated for bulkier substituents because a smaller fraction of phase space contributes to the integral.

The use of stratified sampling[43] can increase the efficiency of the Monte Carlo method. The volume is divided into different subvolumes, and MC points are sampled uniformly across these subvolumes. As the sampling progresses, the contribution of each subvolume to the overall integral is determined. Certain subvolumes contribute more than others to the integral, and the relative number of sample points drawn in each subvolume is adjusted to reflect this, i.e., those subvolumes that make a greater contribution are sampled more frequently.

Care must be taken on dividing the integration domain. For example, division along each coordinate axis in the present case into, for example, 10 strata would produce 10^5, subvolumes which would be expensive to sample (the typical number of MC points used is of the order 10^5 and so this would mean only one MC point would be drawn for each subvolume). In practice, the angles θ_1 and θ_2 turned out to be the most important in determining the configuration integral, and only these angles were stratified. In the presented calculations the range of each angle was divided into 10, producing 10^2 subvolumes.

For the sampling of n subvolumes with different numbers of points, an estimate of the variance of the integral, σ^2, is approximately given by

$$\sigma^2 \approx V\left(\frac{1}{n^2} \sum_{i=1}^{n} Var\,(\langle f \rangle_i) \right) \quad (10)$$

where $Var(\langle f \rangle_i)$ is the variance estimate of f for the subvolume i.

The total number of MC points used in these calculations was 10^5. As expected, volume elements with small values of θ_1 and θ_2, i.e., configurations closest to the reaction coordinate, made the biggest contribution to the configuration integral. Error estimates for the integral were taken to be 2σ. Using stratified sampling, the error estimates were reduced by about 60−80% compared to uniform sampling with the same number of MC points.

III. Dependence of Molecular Properties on *R*

In this section four potential-energy features are discussed: the reaction coordinate potential, conserved mode vibrational frequencies, the fragment geometry, and the transitional mode potential.

III.1. Reaction Coordinate Potential. The rate coefficient $k_\infty(T)$ for the recombination reactions presented here was calculated using eq 6. The reaction coordinate was assumed to be the distance between the centers of mass of the reactants, and the reaction coordinate potential energy was modeled by a Morse function:

$$V(R) = D_0[1 - \exp(-\beta_M(R - R_0))]^2 \qquad (11)$$

The parameters for the Morse function were obtained from thermochemical and spectroscopic data, in particular, the parameter β_M was obtained from the frequency of the C−C stretching mode of the adduct. Some difficulty was experienced with reaction R3—although ν_1 (974 cm^{-1}) is assigned as the C−C stretch in ref 44, when used to calculate the Morse parameter, β_M, a value of 5.8 Å^{-1} was obtained. When this value is used an exceptionally steep potential-energy surface in the transition state region is obtained, and as a consequence this leads to unrealistic rate coefficients. However, this vibrational mode is dominated by motion of the C atoms, and motion of the heavier Cl atoms is very restricted. The reaction coordinate corresponds more closely to the ν_2 (432 cm^{-1}) mode, which is also of A_{1g} symmetry and involves the relative motion of the CCl_3 fragments. This frequency yields a value for β_M of 2.6 Å^{-1}, which is more realistic and was used throughout the rate coefficient calculations.

The TS location $R^\dagger$ for each temperature was found by minimizing k_∞ with respect to R on a 0.10 Å grid of R values. The range of R values varied slightly depending on the kinetically important region for each system: for reaction R1, R = 2.2−7.0 Å; for reaction R2, R = 2.4−7.0 Å; and for reaction R3, R = 2.9−7.0 Å.

III.2. Vibrational Frequencies. To calculate the ratio of the vibrational partition functions, $Q^\dagger_c/Q_{vib,react}$, in eq 6, the conserved mode frequencies, which change somewhat along the reaction coordinate, were obtained by interpolating between reactant and product values:

$$\nu_i(R) = \nu_i^r + (\nu_i^p - \nu_i^r)\exp(-\alpha(R - R_e)) \qquad (12)$$

where R_e is the reaction coordinate value in the product molecule and α is an interpolation parameter. The parameter α was assigned the more-or-less standard value of 1.0 Å^{-1} for all three systems; the effect of varying α was explored only for CH_3 recombination (R1). $\nu_i{}^r$ values are the reactant frequencies which correspond to the normal-mode frequencies in an isolated radical. $\nu_i{}^p$ values are the frequencies of the corresponding product molecule which correlate to $\nu_i{}^r$. $\nu_i{}^p$ values were obtained by averaging two nearly degenerate normal-mode frequencies of the molecule with the same symmetry (either A or E) and the same type of vibration (either stretch or deformation), see Tables 1−3. The resulting four product frequencies $\nu_i{}^p$ were then correlated to the four reactant frequencies with the same symmetry and vibration type. Although the main contribution to the vibrational factor comes from the umbrella motion alone, the correlation of the frequencies along the reaction coordinate was done for all conserved modes, which are listed for the three different recombination reactions in Tables 1−3. The remaining frequencies of the product molecule are the transitional modes and are listed for the three cases in Tables 1−3.

III.3. Fragment Geometry. The change in structure of the fragments as they approach each other, the length of the C−X bond r_{cx}, and the X−C−X bond angle α_{xcx}, was estimated ateach point of the reaction coordinate R by an interpolation:

$$R_{cx}(R) = r_{cx,e}{}^r + [r_{cx,e}{}^p - r_{cx,e}{}^r]\exp[-\alpha(R - R_e)]$$

$$\alpha_{xcx}(R) = \alpha_{xcx,e}{}^r + [\alpha_{xcx,e}{}^p - \alpha_{xcx,e}{}^r]\exp[-\alpha(R - R_e)] \qquad (13)$$

where α = 1.0 Å^{-1}. The change in shape as the fragments approach each other affects the ratio $Q_{fr}{}^\dagger/Q_{fr,}$ however, this factor remains close to unity along the reaction coordinate for all the reactions investigated.

III.4. Transitional Mode Potential. The transitional mode potential, V_{tr}, was calculated using the approximate model described by Wardlaw and Marcus.[4] This model describes the transitional potential as a sum of nonbonding, V_{NB}, and bonding,

TABLE 1: Correlation of Conserved Modes[a] for the CH_3 + CH_3 → C_2H_6 Reaction (cm^{-1}) and Transitional Modes[a] of C_2H_6 (cm^{-1})

a. Correlation of Conserved Modes

C_2H_6				CH_3		
mode	sym	ν_i	$\nu_i{}^p$	mode	sym	$\nu_i{}^r$
ν_1	A_{1g}	2954	2925.0	ν_1	A_1'	3044
ν_5	A_{2u}	2896				
ν_2	A_{1g}	1388	1383.5	ν_2	A_2''	606.5[b]
ν_6	A_{2u}	1379				
ν_7	E_u	2985	2977.0	ν_3	E′	3162
ν_{10}	E_g	2969				
ν_8	E_u	1472	1470.5	ν_4	E′	1396
ν_{11}	E_g	1469				

b. Transitional Modes

mode	sym	ν	description
ν_3	A_{1g}	995	C−C stretch
ν_4	A_{1u}	289	torsion
ν_9	E_u	821	CH_3 rock
ν_{12}	E_g	1206	CH_3 rock

[a] Reference 8. [b] Reference 45. Calculations were also performed with an umbrella mode of 580 cm^{-1} to compare to the Wardlaw−Marcus calculations (ref 4), but no significant difference was observed.

TABLE 2: Correlation of Conserved Modes for the CF_3 + CF_3 → C_2F_6 Reaction (cm^{-1}) and Transitional Modes of C_2F_6[a] (cm^{-1})

a. Correlation of Conserved Modes

C_2F_6[a]				CF_3		
mode	sym	ν_i	$\nu_i{}^p$	mode	sym	$\nu_i{}^r$
ν_1	A_{1g}	1417	1266.5	ν_1	A_1	1088.6[b]
ν_5	A_{2u}	1116				
ν_3	A_{1g}	348	531	ν_2	A_1	701[c]
ν_6	A_{2u}	714				
ν_7	E_u	1250	1250	ν_3	E	1260.2[d]
ν_{10}	E_g	1250				
ν_8	E_g	620	571	ν_4	E	580[e]
ν_{11}	E_u	522				

b. Transitional Modes

mode	sym	ν	description
ν_2	A_{1g}	807	C−C stretch
ν_4	A_{1u}	68	torsion
ν_9	E_g	372	CF_3 rock
ν_{12}	E_u	219	CF_3 rock

[a] Reference 46. [b] Reference 47. [c] Reference 48. [d] Reference 49. [e] Reference 50.

TABLE 3: Correlation of Conserved Modes for the $CCl_3 + CCl_3 \rightarrow C_2Cl_6$ Reaction (cm^{-1}) and Transitional Modes of C_2Cl_6[a] (cm^{-1})

a. Correlation of Conserved Modes

C_2Cl_6[a]				CCl_3		
mode	sym	ν_i	$\nu_i{}^p$	mode	sym	$\nu_i{}^r$
ν_1	A_{1g}	974	827.5	ν_1	A_1	674[b]
ν_5	A_{2u}	681				
ν_3	A_{1g}	288	330.5	ν_2	A_1	338[c]
ν_6	A_{2u}	373				
ν_7	E_g	854	817.0	ν_3	E	898[b]
ν_{10}	E_u	780				
ν_8	E_g	341	308.5	ν_4	E	272[c]
ν_{11}	E_u	276				

b. Transitional Modes

mode	sym	ν	description
ν_2	A_{1g}	432	C−C stretch
ν_4	A_{1u}	77	torsion
ν_9	E_g	223	CCl_3 rock
ν_{12}	E_u	167	CCl_3 rock

[a] Reference 44. [b] Reference 51. [c] Reference 52.

TABLE 4: Potential-Energy Parameters for the $CX_3\cdots CX_3$ System ($\alpha = 1.0$ Å^{-1})

parameter	X = H	ref	X = F	ref	X = Cl	ref
			C_2X_6			
$r_{CX,e}$ [Å]	1.111	4	1.326	54	1.769	61
$r_{CC,e}$ [Å]	1.533	4	1.545	54	1.56	61
$\alpha_{CCX,e}$ [deg]					110.0	61
$\alpha_{XCX,e}$ [deg]	107.3	4	109.5	54	108.9	*g*
$D_{0,CC}$ [kJ mol^{-1}]	366.5	4	406.5	*c*	286.3	*c*
D_{CC} [kJ mol^{-1}]	404.2	4	418.4	*d*	294.7	*d*
R_e [Å]	1.696	4	2.274	*e*	2.645	*e*
β_{CC} [Å^{-1}]	1.80	4	3.15	*f*	2.57	*f*
$D_{CC}{}^{ef}$ [kJ mol^{-1}]	810.9	*a*	806.3	*a*	390.3	*a*
$\beta_{CC}{}^{ef}$ [Å^{-1}]	1.82	*a*	3.94	*a*	4.73	*a*
$r_{CC}{}^{ef}$ [Å]	1.15	*a*	1.52	*a*	1.88	*a*
ν_{CC} [cm^{-1}]	995	8	807	46	432	44
			CX_3			
$r_{CX,e}$ [Å]	1.079	4	1.318	60	1.714	62
$\alpha_{XCX,e}$ [deg]	120	4	110.7	60	117.4	62
			$CX_3\cdots CX_3$			
ϵ_{X-X} [kJ mol^{-1}]	0.042	53	1.276	53	1.276	53
ϵ_{C-C} [kJ mol^{-1}]	0.397	53	0.397	53	0.397	53
ϵ_{C-X} [kJ mol^{-1}]	0.130	*b*	0.711	*b*	0.711	*b*
$r_{X-X,0}$ [Å]	3.37	53	3.285	53	3.915	53
$r_{C-C,0}$ [Å]	3.88	53	3.880	53	3.880	53
$r_{C-X,0}$ [Å]	3.62	*b*	3.582	*b*	3.897	*b*

[a] Obtained from a nonlinear least-squares fitting as described in the text. The effective Morse parameters for $\alpha = 0.7$ Å^{-1} in the $CH_3\cdots CH_3$ system are the same as those for $\alpha = 1.0$ Å^{-1} except for $D_{CC}{}^{ef} = 795.0$ kJ mol^{-1}. [b] $\epsilon_{C-X} = (\epsilon_{X-X}\,\epsilon_{C-C})^{1/2}$; $r_{C-X,0} = 1/2(r_{X-X,0} + r_{C-C,0})$. [c] $D_{0,CC}$ calculated from $\Delta H_f°$ of C_2X_6 and CX_3. $\Delta H_f{}^{298}$ of C_2X_6 obtained from ref 55. $\Delta H_f{}^{298}$ of CH_3 and CF_3 obtained from ref 56. $\Delta H_f{}^{298}$ of CCl_3 obtained from ref 57. $\Delta H_f{}^{298}$ converted to $\Delta H_f{}^0$ with $H° - H^{298}$ from refs 58 and 59. [d] $D_{cc} = D_{0,CC} + E_{zr} - E_{zp}$ where E_{zr} and E_{zp} are determined by the normal-mode frequencies of C_2X_6 and CX_3. [e] Determined from the equilibrium geometry and the atomic masses of C_2X_6. [f] $\beta_{CC} = (\mu/2D_{CC})^{1/2}2\pi c\nu_{CC}$. [g] Calculated from $r_{CCl,e}$ and $\alpha_{CCCl,e}$ of C_2Cl_6.

V_B, interactions:

$$V_{tr} = V_{NB} + V_B \tag{14}$$

All the parameters needed to determine V_{tr} for all three cases are listed in Table 4.

A Lennard−Jones potential, V_{LJ}, was used to describe the interactions between all nonbonded C−X and X−X pairs; the C−C interactions were excluded, and Coulomb interactions were disregarded.[63] V_{LJ} is given by $V_{LJ} = \epsilon[(r_0/r)^{12} - 2(r_0/r)^6]$. The equation for the nonbonded potential V_{NB} is as follows:

$$V_{NB} = \sum_{i,j=1}^{4} V_{LJ}(r_{ij}) \tag{15}$$

where i is an index over the atoms on the first CX_3 fragment, j is an index over atoms on the second fragment, and r_{ij} are the distances between the nonbonded atoms. The exclusion of the C−C nonbonded interaction was effected by setting the ϵ parameter to zero for this interaction. The Lennard−Jones parameters were taken from the DREIDING potential.[53]

The potential for the C−C bond, V_B, was represented by a Morse function modified by an orientational factor to account for bonding orbital overlap:

$$V_B = V_M{}^{ef}(r_{cc}) \cos^2 \tau_1 \cos^2 \tau_2 \tag{16}$$

where $V_M{}^{ef}$ is an effective potential given by

$$V_M{}^{ef} = D_{cc}{}^{ef}\{1 - \exp[-\beta_{cc}{}^{ef}(r_{cc} - r_{cc,e}{}^{ef})]\}^2 - D_{cc}{}^{ef} \tag{17}$$

Note that $V_M{}^{ef}$ is a function of r_{cc} (the distance between the carbon atoms) and not the reaction coordinate. The angles τ_1 and τ_2 are between r_{cc} and the C_3 axes of the respective fragments. The angles τ_1 and τ_2 are determined by the vector definition of the cosine:

$$\cos \tau_i = \frac{\mathbf{u_i}\cdot\mathbf{r_{cc}}}{|\mathbf{u_i}||\mathbf{r_{cc}}|} \tag{18}$$

where $\mathbf{r_{cc}}$ is the vector between the carbon atoms and $\mathbf{u_i}$ is a vector along the C_3 axis of the ith fragment. τ_1 and τ_2 are functions of θ_1, θ_2, and χ. (It should be noted that τ_1 and τ_2 are not the same as θ_1 and θ_2 since $\mathbf{r_{cc}}$ and the vector joining the centers of mass of the fragments are, in general, not the same.)

The effective Morse parameters in eq 17 are introduced so that the complete transitional mode potential V_{tr} (eq 14), when evaluated at the "local" equilibrium configuration ($\theta_1 = \theta_2 = \phi_1 = \chi = 0°$ and $\phi_2 = 60°$, i.e., staggered arrangement with the nonplanar fragments splayed away from each other as in ethane) yields the desired Morse reaction coordinate potential (eq 11). These three parameters were obtained by least-squares fitting using a Marquardt algorithm.[64]

For the recombination reaction R1, the root-mean-square deviation of V_{tr} from $V(R)$ in the r_{cc}-interval 2.2−7.0 Å, where the transition states occur for the temperatures considered, was only 0.17 kJ mol^{-1}. For the other two recombination reactions, the deviation of V_{tr} from $V(R)$ was larger. The interval used for the $2CF_3 \rightarrow C_2F_6$ recombination was 2.4−7.0 Å and for the $2CCl_3 \rightarrow C_2Cl_6$ recombination 2.9−7.0 Å, and the deviations were 2.55 and 2.59 kJ mol^{-1}, respectively.

The simplified model for V_{tr} has limitations, the biggest practical problem being the determination of the effective Morse parameters in eq 17, which are obtained by fitting the sum ($V_{NB} + V_B$) to a known C−C Morse function. Since the biggest deviations from the fitted function occur at shorter separation distances, where the nonbonding interactions are large, the effective Morse parameters depend strongly on the interval of the fit. This problem is accentuated for the $CF_3\cdots CF_3$ (R2) and $CCl_3\cdots CCl_3$ (R3) systems because of the stronger nonbonded interactions arising when halogens are substituted for hydrogen. (The ϵ_{C-X} (X = F, Cl) Lennard−Jones parameter

TABLE 5: Rate Coefficients $k_\infty(T)$ for the Reaction $CH_3 + CH_3 \rightarrow C_2H_6$ ($\alpha = 1.0$ Å^{-1})

temp [K]	$R^\dagger$ [Å]	k_∞ [10^{-11} cm^3 molecule^{-1} s^{-1}]
300	4.26	8.93 ± 0.02
400	4.06	8.68 ± 0.02
500	3.87	8.14 ± 0.02
600	3.67	7.55 ± 0.03
800	3.47	6.39 ± 0.02
1000	3.37	5.31 ± 0.02
2000	2.89	2.47 ± 0.01

TABLE 6: Rate Coefficients $k_\infty(T)$ for the Reaction $CH_3 + CH_3 \rightarrow C_2H_6$ ($\alpha = 0.7$ Å^{-1})

temp [K]	$R^\dagger$ [Å]	k_∞ [10^{-11} cm^3 molecule^{-1} s^{-1}]
300	4.26	7.20 ± 0.01
400	3.96	7.09 ± 0.02
500	3.87	6.64 ± 0.02
600	3.67	6.14 ± 0.02
800	3.57	5.16 ± 0.02
1000	3.38	4.27 ± 0.02
2000	2.98	1.99 ± 0.01

TABLE 7: Rate Coefficients $k_\infty(T)$ for the Reaction $CF_3 + CF_3 \rightarrow C_2F_6$ ($\alpha = 1.0$ Å^{-1})

temp [K]	$R^\dagger$ [Å]	k_∞ [10^{-12} cm^3 molecule^{-1} s^{-1}]
300	3.62	13.42 ± 0.14
400	3.53	9.31 ± 0.09
500	3.43	7.37 ± 0.07
600	3.43	6.15 ± 0.06
800	3.34	4.63 ± 0.04
1000	3.24	3.68 ± 0.03
2000	3.06	2.00 ± 0.02

is $\sim 6\epsilon_{C-H}$, and ϵ_{X-X} is $\sim 30\epsilon_{H-H}$.) As the effective Morse parameters directly influence the transitional mode potential and, hence, the rate coefficient, it is vital to have a consistent method of determining them in order to make reliable predictions for the temperature dependence and a meaningful comparison between the different reaction systems. The interval we eventually chose for the fit included all values of R, which were necessary to find the TS for all temperatures (i.e., $T = 300-2000$ K), but did not include the very short separation distances, where the deviations had the highest values. Thus, the interval for reaction R1 was $R = 2.2-7.0$ Å, for reaction R2 $R = 2.4-7.0$ Å, and for reaction R3 $R = 2.9-7.0$ Å. Some difficulty was experienced in fitting the potential for reaction R3, since there are multiple minima in the χ^2 surface, depending on the initial values of D_{CC}^{ef}, β_{CC}^{ef}, and r_{CC}^{ef} in the nonlinear least-squares fit. However, the rate coefficients are relatively insensitive to the particular set of minimum parameters used.

IV. Results and Discussion

IV.1. Temperature Dependence. The calculated values of the high-pressure limiting rate coefficients, $k_\infty(T)$, for the reactions R1, R2, and R3 and the corresponding locations of $R^\dagger$ are listed in Tables 5−8. In most cases the interpolation parameter α (eq 12) was chosen to be 1.0 Å^{-1}. For comparison with the calculations of Wagner and Wardlaw,[19] the rate coefficient $k_\infty(T)$ for reaction R1 was also calculated with $\alpha = 0.7$ Å^{-1} (Table 6).

All three reaction systems exhibit a negative temperature dependence. On going from CH_3 to CF_3 to CCl_3 recombination, i.e., as the substituents become increasingly bulky, the rate coefficient at a given temperature decreases and the negative temperature dependence becomes stronger. The increasing steepness in the negative temperature dependence is illustrated in Figure 1, which shows the rate coefficients, k_∞, relative to the 300 K value for the three different systems, as a function of temperature. Changing $\alpha = 1.0$ Å^{-1} to $\alpha = 0.7$ Å^{-1} in reaction R1, decreases the rate coefficient by ~20% across the studied temperature range but does not have an effect on the temperature dependence (Tables 5 and 6).

TABLE 8: Rate Coefficients $k_\infty(T)$ for the Reaction $CCl_3 + CCl_3 \rightarrow C_2Cl_6$ ($\alpha = 1.0$ Å^{-1})

temp [K]	$R^\dagger$ [Å]	k_∞ [10^{-12} cm^3 molecule^{-1} s^{-1}]
300	3.99	4.17 ± 0.06
400	3.82	3.00 ± 0.04
500	3.65	2.33 ± 0.03
600	3.57	1.84 ± 0.02
800	3.49	1.18 ± 0.01
1000	3.40	0.855 ± 0.008
2000	3.23	0.308 ± 0.003

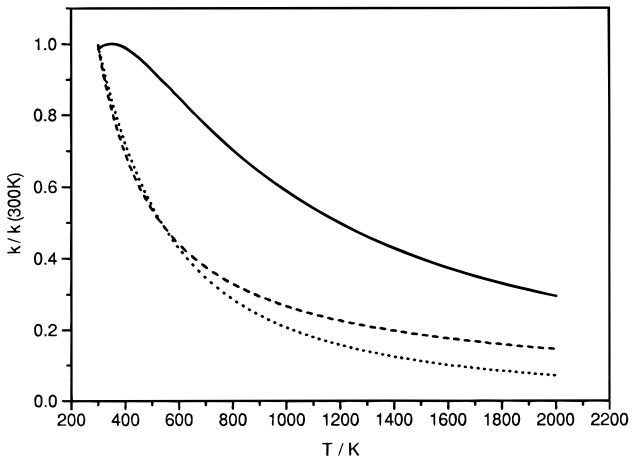

Figure 1. Temperature dependence of the rate coefficients for the reactions $CH_3 + CH_3$ (—), $CF_3 + CF_3$ (- - -), and $CCl_3 + CCl_3$ (·····).

It is of interest to investigate the factors that affect the rate coefficient and its dependence on temperature. The rate coefficient is given by eq 6 and can also be written in the form:

$$k_\infty(T) = g_e \frac{1}{\beta h} \frac{\sigma}{\sigma^\dagger} \frac{1}{Q_{trans}} e^{-\beta V^\dagger} Q_{pd} \Omega_{vib} \Omega_{rot} \Gamma \qquad (19)$$

There are five factors that depend on R and, therefore, potentially contribute to the location of the TS and to the dependence of k_∞ on temperature. The changes in the contributing factors for reaction R1 at 2000 K are shown in a logarithmic plot in Figure 2 as a function of the reaction coordinate. These factors (already explained in more detail in section II) are Γ, the hindering function in the form of the configuration integral; $e^{-\beta V}$, where V is the potential along the reaction coordinate; Q_{pd}, the pseudodiatomic partition function for the orbiting motion of the two fragments; Ω_{vib}, the quotient of the vibrational partition functions, and Ω_{rot}, the quotient of the free rotor partition functions. Ω_{rot} is almost constant and close to unity along the reaction coordinate and, therefore, does not have a significant effect on the location of the TS or the magnitude or temperature dependence of k_∞. Q_{pd} is proportional to R^2, and Ω_{vib} also increases with R. The most dramatic changes are found for the hindering function Γ, which increases, and the term $e^{-\beta V}$, which decreases as R increases. It is, therefore, primarily the interaction between the factors Γ and $e^{-\beta V}$ that most influences

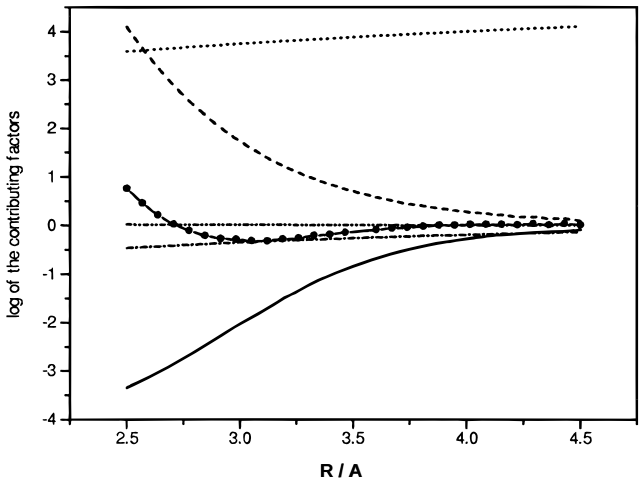

Figure 2. Logarithmic plot of the contributing factors to the rate coefficient as a function of the distance R for the reaction $CH_3 + CH_3$ at 2000 K: (—) Γ; (- - -) $e^{-\beta V}$; (•••••) Q_{pd}; (-•-•-) Ω_{vib}; (-••-••)Ω_{rot}; (●) $\Gamma e^{-\beta V}$.

TABLE 9: Components of the Ratio $P = k_\infty(X)/k_\infty(H)$ for the Reactions $CX_3 + CX_3 \rightarrow C_2X_6$

X	$(R^\dagger_X/R^\dagger_H)^2$	$(\mu_H/\mu_X)^{1/2}$	$(e^{-\beta V}\Gamma)_X/(e^{-\beta V}\Gamma)_H$	$\Omega_{vib,X}/\Omega_{vib,H}$	$\Omega_{rot,X}/\Omega_{rot,H}$	P
			300 K			
F	0.72	0.47	0.22	1.04	0.98	0.152
Cl	0.88	0.36	0.069	1.10	0.97	0.047
			2000 K			
F	1.12	0.47	0.048	1.65	0.96	0.080
Cl	1.25	0.36	0.010	1.46	0.95	0.012

the location of the TS and hence the rate coefficient. The product $\Gamma e^{-\beta V}$ is also included in Figure 2; the minimum of this curve is the approximate location of the TS at 2000 K.

Equation 19 can be rewritten:

$$k_\infty(T) = g_e \frac{\sigma}{\sigma^\dagger} \pi (R^\dagger)^2 \left(\frac{8kT}{\pi\mu}\right)^{1/2} \Omega_{vib}\Omega_{rot} e^{-\beta V^\dagger}\Gamma \qquad (20)$$

where $R^\dagger$ is the location of the TS at a given temperature. This form emphasizes the connection between the TS and collision theories and also allows further exploration of the importance of the product $e^{-\beta V}\Gamma$. Consider the ratio, P, of the rate coefficients for the reactions R2 and R3 versus that for R1, i.e., $P = k_\infty(X)/k_\infty(H)$, where X and H represent the substituents on the reacting fragments and X is either F or Cl

$$P = \left(\frac{C_X}{C_H}\right)\left(\frac{R_X^\dagger}{R_H^\dagger}\right)^2\left(\frac{\mu_H}{\mu_X}\right)^{1/2}\left(\frac{(e^{-\beta V}\Gamma)_X}{(e^{-\beta V}\Gamma)_H}\right)\left(\frac{\Omega_{vib,X}}{\Omega_{vib,H}}\right)\left(\frac{\Omega_{rot,X}}{\Omega_H}\right) \qquad (21)$$

where C_X and C_H represent the symmetry number ratios. The radicals CF_3 and CCl_3 are nonplanar in the TS and as separated reactants and were each assigned a symmetry number of 3 for both TS and reactants. As a consequence, C_X for X = F or Cl is always unity. The case of CH_3 is somewhat more complex: the separated fragments are planar and have a symmetry number of 6 each or 36 for the reactant pair. The methyl fragments are assumed planar at the TS, and hence, the overall symmetry for the TS is $2 \times 36 = 72$. The extra factor of 2 arises from molecular symmetry considerations[65] for planar fragments, as each distinct relative orientation of the fragments at the TS can be obtained from two sets of the orientation angles θ_1, θ_2, ϕ_1, ϕ_2, and χ. Thus, $C_H = 36/72 = 1/2$. Table 9 lists the component factors of P for X = F and Cl and temperatures of

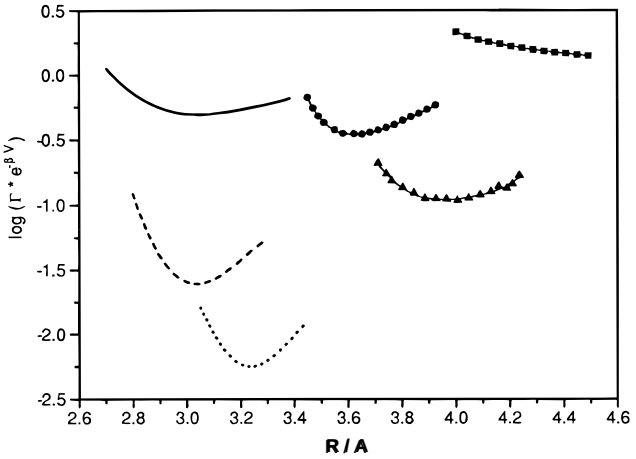

Figure 3. Product of the contributing factors $e^{-\beta V}$ and Γ in a logarithmic plot: (■) $CH_3 + CH_3$ at 300 K; (—) $CH_3 + CH_3$ at 2000 K; (●) $CF_3 + CF_3$ at 300 K; (- - -) $CF_3 + CF_3$ at 2000 K; (▲) $CCl_3 + CCl_3$ at 300 K; (•••••) $CCl_3 + CCl_3$ at 2000 K.

TABLE 10: Components of the Ratio $Z = k_\infty(300)/k_\infty(2000)$ for the Reaction $CX_3 + CX_3 \rightarrow C_2X_6$

X	$(R^\dagger_{300}/R^\dagger_{2000})^2$	$(e^{-\beta V}\Gamma)_{300}/(e^{-\beta V}\Gamma)_{2000}$	$\Omega_{vib,300}/\Omega_{vib,2000}$	$\Omega_{rot,300}/\Omega_{rot,2000}$	Z
H	2.17	2.83	1.54	0.98	3.59
F	1.40	12.6	0.97	1.00	6.63
Cl	1.53	19.9	1.15	1.01	13.7

300 and 2000 K. This table shows that the ratio of the factors $e^{-\beta V}\Gamma$ is primarily responsible for the decrease in rate coefficient with the size of X, although the mass term is also significant. Another useful comparison, based on eq 20, is to consider the ratio, Z, of the rate coefficients for the same reaction at two different temperatures, e.g., $Z = k_\infty(300\text{ K})/k_\infty(2000\text{ K})$:

$$Z = \left(\frac{300}{2000}\right)^{1/2}\left(\frac{R_{300}^\dagger}{R_{2000}^\dagger}\right)^2\left(\frac{(e^{-\beta V}\Gamma)_{300}}{(e^{-\beta V}\Gamma)_{2000}}\right)\left(\frac{\Omega_{vib,300}}{\Omega_{vib,2000}}\right)\left(\frac{\Omega_{rot,300}}{\Omega_{rot,2000}}\right) \qquad (22)$$

The components of Z for the three reactions are listed in Table 10. It is clear that the product $e^{-\beta V}\Gamma$ is the dominant factor in determining the temperature dependence for both the CF_3 and CCl_3 recombination reactions. For the CH_3 recombination, the effect of the product $e^{-\beta V}\Gamma$ is less pronounced and the other factors, in particular R^2 and Ω_{vib}, are significant.

The interplay between the factors Γ and $e^{-\beta V}$ for all three reaction systems, at both 300 and 2000 K, is shown in Figure 3. Except for reaction R1 at 300 K, all the curves exhibit a minimum, emphasizing the role of Γ and $e^{-\beta V}$ in determining the position of the TS and, hence, the magnitude of k_∞ and its temperature dependence. For reaction R1 at 300 K, a minimum is obtained if the other factors, i.e., R^2 and Ω_{vib}, are included (see above), however, as the temperature increases, a minimum is obtained without the extra factors. The minima of the curves show the approximate location of the TS at the corresponding temperature. The minima at 2000 K are clearly at a shorter R compared to those at 300 K. This is in accordance with the TS getting tighter with higher temperatures, an effect which has been observed previously, e.g., by Rai and Truhlar.[9] Also, for a specific reaction, the 2000 K curve has a lower minimum than the equivalent curve at 300 K, as shown earlier in Table 10, and this effect is the primary cause of the decrease in the rate coefficient with temperature.

It is worth investigating the factor Γ more closely. The hindering function Γ is given by eq 7 and depends exclusively

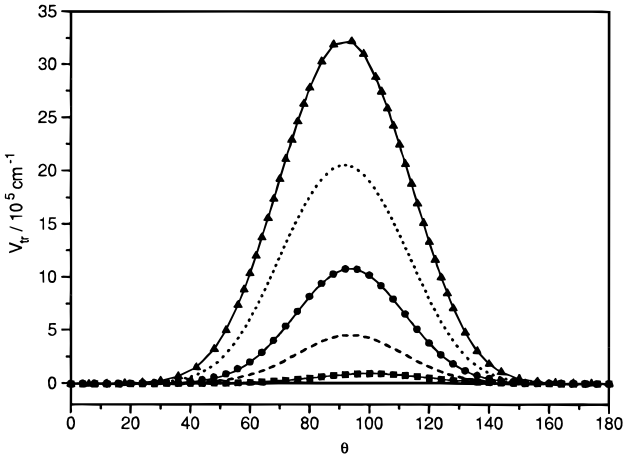

Figure 4. Transitional mode potential V_{tr} as a function of the polar angle θ at the location of the TS corresponding to 1000 and 2000 K: (—) $CH_3 + CH_3$ at 1000 K; (■) $CH_3 + CH_3$ at 2000 K; (- - -) $CF_3 + CF_3$ at 1000 K; (●) $CF_3 + CF_3$ at 2000 K; (·····) $CCl_3 + CCl_3$ at 1000 K; (▲) $CCl_3 + CCl_3$ at 2000 K.

on V_{tr}, which is described in detail in section III. In Figure 4, V_{tr} is plotted versus the polar angle θ for the three different recombination reactions at the locations of the TS corresponding to 1000 and 2000 K. The dihedral angle χ and the axial angles $\phi_{1,2}$ are fixed to $\chi = \phi_1 = 0°$ and $\phi_2 = 60°$. The polar angle θ is varied from 0° to 180°. θ_1 and θ_2 for the two fragments are varied simultaneously by the same factor. They are defined such that at the 0° value the fragments are splayed away from each other and while θ_i is varied they rotate in opposite directions so that they are mirror images of each other and θ_1 and θ_2 have the same value. The distance R between the two fragments is kept constant and is the location of the canonical FTST transition state at the corresponding temperature. As expected for all three systems, the V_{tr} have maxima close to $\theta = 90°$, which corresponds to the situation where the C_3 axes of the fragments are parallel and perpendicular to the vector between the centers of mass—this orientation has an increased repulsive nonbonded interaction and minimum bonding orbital overlap. Comparing the three different systems the peak of V_{tr} gets higher and broader in the series CH_3 to CF_3 to CCl_3 recombination: the increasingly repulsive V_{tr} is a consequence of the larger substituents on the reacting fragments. At 1000 K, where the locations of the transition states are at larger R, compared to those at 2000 K, the repulsion and, therefore, V_{tr} are smaller.

Figure 5 shows V_{tr} as a function of the polar angles θ_1 and θ_2 in a contour plot for reaction R1 at $R = 2.9$ Å, which is the location of the TS at $T = 2000$ K. The conditions are as in Figure 4, which is a diagonal cross-cut of the contour plot. Although Figure 5 seems to be symmetric, it is not quite so because V_{tr} does not peak exactly at $\theta = 90°$ but at about $\theta = 100°$, the CH_3 radicals are not planar but have a splayed structure which depends on R. In Figure 6, V_{tr} is displayed as a function of the polar angle θ_2 and the axial angle ϕ_2 for reaction R1 at R=2.9 Å. While one fragment is fixed ($\theta_1 = \phi_1 = \chi = 0$), the other fragment rotates about θ_2 from 0° to 180° and about ϕ_2 from 0° to 120°. The potential exhibits a maximum at approximately $\theta_2 = 100°$ and $\phi_2 = 30°$ and a saddle point at $\theta_2 = 100°$ and $\phi_2 = 90°$. Comparison with Figure 2 in ref 14 shows that this part of the potential energy surface is qualitatively similar to that for the reaction $CH_3 + H \rightarrow CH_4$ apart from a shift of 30° in ϕ_2.

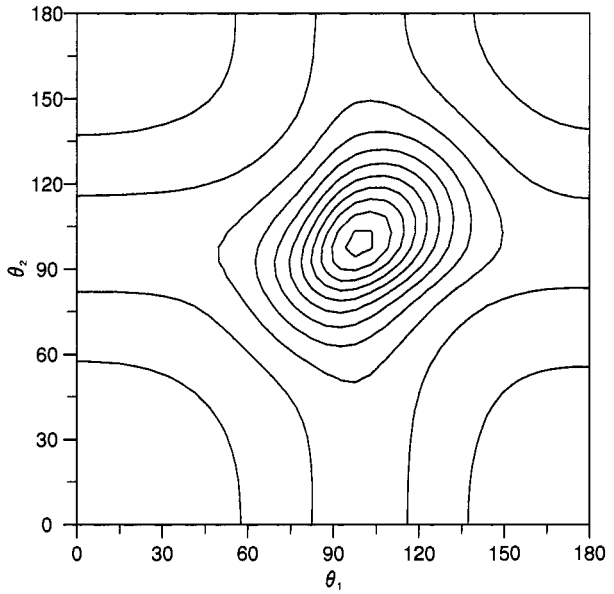

Figure 5. Contour plot of V_{tr} at $R = 2.9$ Å as a function of θ_1 and θ_2 for the reaction $CH_3 + CH_3$. Contours are every 8500 cm^{-1} starting from 0.

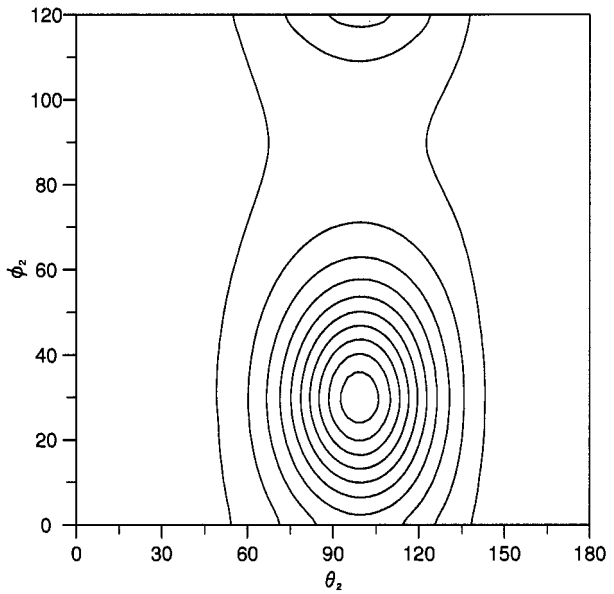

Figure 6. Contour plot of V_{tr} at $R = 2.9$ Å as a function of θ_2 and ϕ_2 for the reaction $CH_3 + CH_3$. Contours are every 5500 cm^{-1} starting from 0.

For the other two reaction systems, R2 and R3, similar contour plots were made for V_{tr}. While the shape of the contours was comparable to that for reaction R1, the height of the maximum for V_{tr} was increased substantially the larger the substituents on the carbon atoms became. These plots show that V_{tr} gets more repulsive for bulkier fragment substituents, reducing the $e^{-\beta V_{tr}}$ term in the hindering function Γ and the rate coefficient. This effect becomes more dramatic at higher temperatures where the location of the TS is at shorter R.

IV.2. Comparison with Experimental and Other Theoretical Studies. (a) $CH_3 + CH_3$. The recombination of CH_3 radicals has been the subject of numerous experimental and theoretical studies.[15−21] The results of the present investigation of the high-pressure limiting rate coefficient, k_∞, as a function of temperature are compared with some of these studies in Figure 7. There are six curves in Figure 7: canonically derived

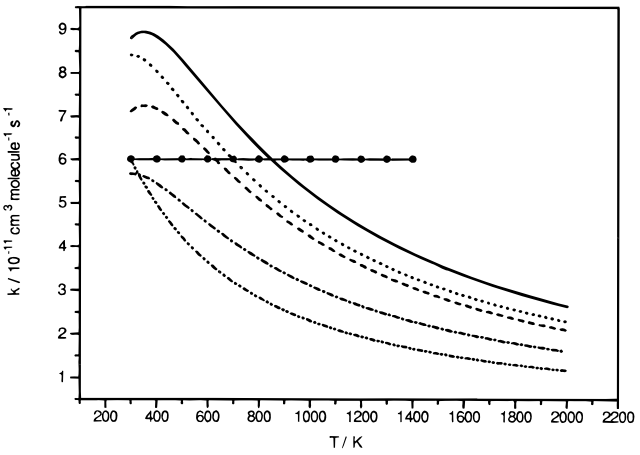

Figure 7. Comparison of the high-pressure limiting rate coefficient for the CH_3 recombination versus temperature: (—) this work (α = 1.0 Å^{-1}); (- - -) this work (α = 0.7 Å^{-1}); (•••••) ref 4 (α = 1.0 Å^{-1}); (-•-•-) ref 19 (α = 0.7 Å^{-1}); (-•••-•••) ref 67; (●) ref 70.

values by Wardlaw and Marcus for α = 1.0 Å^{-1};[4] microcanonically derived values by Wardlaw and Wagner for α = 0.7 Å^{-1} obtained from fits to experimental data;[19] fits to experimental data by Troe[66] based on the constant value for k_∞ suggested by the SACM;[21] fits to experimental data by Robertson et al.;[67] canonically derived values from this work for α = 1.0 Å^{-1} and 0.7 Å^{-1}. A smaller value of α leads to a decrease in the rate coefficient but does not affect the temperature dependence.

The fit to experimental $k(p,T)$ obtained by Robertson et al.[67] used a master equation/inverse Laplace transform method, which has the advantage that details of the PES are not required. The experimental data were taken from refs 15−18 and 68. Similar analyses of the available experimental data also require negative temperature dependencies in k_∞[69,70] Figure 7 shows that the experimentally derived values, obtained by extrapolation of the fit in ref 67 to high pressure, lie below the results from this work and from the other theoretical studies.

The original application of FTST to this system was by Wardlaw and Marcus (WM),[4] who calculated rate coefficients in two ways: in the first, microcanonically derived rate coefficients (denoted $k_{\infty,\mu}^{(WM)}$) were obtained by minimizing the microcanonical rate coefficients with respect to the reaction coordinate and then forming the standard average. In the second, canonically derived rate coefficients (denoted $k_\infty^{(WM)}$) were obtained by averaging the microcanonical rate coefficients first and then minimizing this average with respect to the reaction coordinate. A temperature range of 300−2000 K and values of the interpolation parameter α of 0.8 and 1.0 Å^{-1} were used in these calculations. The canonically derived results are larger than, and an upper bound to, the "true" microcanonically derived rate coefficients, because at the microcanonical level the location of the TS is a function of energy, while at the canonical level the same TS location is used for all energies at a given temperature. The WM results for α = 1.0 Å^{-1} are listed in the second and third columns of Table 11. WM used a transitional mode potential ($V_{tr}^{(WM)}$) identical to that described in section III and in Table 4 with the exception of the effective Morse parameters (D_{CC}^{ef}, β_{CC}^{ef}, r_{CC}^{ef}). Their values differ slightly from those obtained in this work due to the different fitting ranges: 1.75−6.78 Å for WM versus 2.2−7.0 Å here. For example for α = 1.0 Å^{-1}, WM obtained (D_{CC}^{ef}, β_{CC}^{ef}, r_{CC}^{ef}) = (847.3 kJ mol^{-1}, 1.90 Å^{-1}, 1.18 Å) whereas we obtained (810.9 kJ mol^{-1}, 1.83 Å^{-1}, 1.15 Å). WM also used the same interpolation with the same reactant- and product-limiting values

TABLE 11: Comparison of Wardlaw−Marcus Treatment to Current Work: $k_\infty(T)$ for the Reaction $CH_3 + CH_3 \rightarrow C_2H_6$ (α = 1.0 Å^{-1})[a]

	Wardlaw−Marcus			this work	
temp [K]	$k_{\infty,\mu}^{(WM)}$	$k_\infty^{(WM)}$	$k_\infty^{(WM)}/k_{\infty,\mu}^{(WM)}$	k_∞	$k_\infty/k_\infty^{(WM)}$
300	7.19	8.44	1.17	8.93	1.06
500	6.09	7.27	1.19	8.14	1.12
1000	3.94	4.63	1.18	5.31	1.15
2000	1.81	2.19	1.21	2.47	1.13

[a] All rate coefficients are in units of 10^{-11} cm^3 molecule^{-1} s^{-1}.

for the reaction coordinate dependence of the conserved mode frequencies and the fragment structure. The canonically calculated rate coefficients from the WM treatment[4] for α = 1.0 Å^{-1} are also shown in Figure 7. In the WM approach, the momenta were not treated analytically but included directly in the MC integration, greatly increasing the computational effort required. A further difficulty was experienced when the energy integration, required to obtain the canonical TS partition function, was introduced into the MC procedure, leading to unacceptably large standard deviations, increasing the computational requirements still further. Consequently, a similar amount of CPU time was used in evaluating both canonical and microcanonical rate coefficients. In the present approach, the integration over energy to give the canonical TS partition function is treated implicitly (because the Laplace transform is performed before integration begins) and the computational effort is much less for the present canonical approach. The ratio $k_\infty^{(WM)}/k_{\infty,\mu}^{(WM)}$ in column 4 of Table 11 indicates that the overestimation of the rate coefficient provided by a canonical treatment relative to the (correct) microcanonically based treatment is very close to 20% on the 300−2000 K temperature range. We shall, therefore, use a factor of 1.20 to convert, in approximate fashion, between canonically and microcanonically based rate coefficients obtained from other treatments.

Subsequently, Wagner and Wardlaw (WW)[19] obtained optimized microcanonically based, pressure-dependent rate coefficients by fitting to the extensive set of experimentally determined rate coefficients measured by Macpherson et al.[15] and Slagle et al.[16] The WW treatment employed microcanonical FTST recombination rate coefficients plus the Troe strong collision model[71,72] with weak collision corrections to describe the pressure-dependent effect of collisions of energized C_2H_6* with the buffer gas argon. WW used the same transitional mode potential ($V_{tr}^{(WM)}$) and the same reaction coordinate dependence for the conserved mode frequencies and the fragment structure as WM. Adjustable parameters in their fit were the interpolation parameter α and the average total energy change $\langle\Delta E_{tot}\rangle$ in energized C_2H_6* per buffer gas collision. The parameter values giving the best fit to the measured rate coefficients were found to be $\alpha = 0.7 \pm 0.13$ Å^{-1} and $\langle\Delta E_{tot}\rangle = -205 \pm 65$ cm^{-1}. The high-pressure limiting rate coefficients obtained from the WW treatment (denoted $k_{\infty,\mu}^{(WW)}$) are listed in column 2 of Table 12 and plotted in Figure 7; note that in this limit there is dependence only on α and not on $\langle\Delta E_{tot}\rangle$. Column 3 provides an estimate of the associated canonical rate coefficient (denoted $k_\infty^{(WW)}$), obtained by multiplying $k_{\infty,\mu}^{(WW)}$ by the conversion factor (1.20) proposed above.

The right-hand-most columns of Tables 11 and 12 provide a comparison of our results for the canonically derived high-pressure rate coefficient to the corresponding results of WM and WW, respectively. Comparisons are made at those temperatures in common with these earlier treatments. Note that the WM and WW results are compared to our results for α =

TABLE 12: Comparison of Wardlaw−Wagner Treatment to Current Work: $k_\infty(T)$ for the Reaction $CH_3 + CH_3 \rightarrow C_2H_6$ ($\alpha = 0.7$ Å^{-1})[a]

Wardlaw−Wagner			this work		
temp [K]	$k_{\infty,\mu}^{(WW)}$	$k_\infty^{(WW)} \approx 1.2k_{\infty,\mu}^{(WW)}$	temp [K]	$k_{\infty/}$	$k_{\infty}/k_\infty^{(WW)}$
296	5.78	6.94	300	7.20	1.04
407	5.35	6.42	400	7.09	1.10
577	4.78	5.74	600	6.14	1.07
810	3.76	4.51	800	5.16	1.14
2000	1.47	1.76	2000	1.99	1.13

[a] All rate coefficients are in units of 10^{-11} cm^3 molecule^{-1} s^{-1}.

1.0 Å^{-1} and 0.7 Å^{-1}, respectively. At all temperatures considered, our predictions for k_∞ exceed those of WM and WW by 4−14% with the average excess being ca. 10% on the 300−2000 K temperature range. This discrepancy is likely attributable to the slightly different transitional mode potentials: V_{tr} for this work versus $V_{tr}^{(WM)}$ for WM and WW. The observation that our results overestimate the results of two related but separate treatments at two different values of α by essentially the same factor is encouraging: it suggests that the three treatments are internally consistent and that their numerical implementation is free from systematic error. All three treatments give a similar negative temperature dependence for the recombination rate coefficient of this reaction.

Troe's temperature-independent value for k_∞ agrees with the WW value at 300 K, a consequence of fitting α to the experimental data at 300 K, where the high-pressure limit is best defined. In the original version of SACM, α was used as a universal parameter to link both the conserved and transitional modes in reactants and products. It thus implicitly contains information on V_{tr}. The present analysis demonstrates the great sensitivity of k_∞ to Γ and, hence, to V_{tr}; it is unlikely that a simple parametrization will capture the comparatively subtle temperature dependence of k_∞ for reaction R1. At the same time, it must be recognized that the form of V_{tr} used in the present analysis, while representative, has its limitations and an analysis based on a more reliable ab initio potential is needed.

(b) $CF_3 + CF_3$. For the CF_3 recombination reaction there has been, to our knowledge, no report of a directly measured temperature dependence of the limiting high-pressure rate coefficient. The high-pressure limiting rate coefficient near room temperature has been measured by numerous groups.[22−36] The results vary by more than an order of magnitude ($(2 \times 10^{-12})-(4.5 \times 10^{-11})$ cm^3 molecule^{-1} s^{-1}). Hranisavljevic and Michael[37] have assessed these results and concluded that there is no consensus room-temperature value. These authors did, however, provide an ad hoc estimate of 4.5×10^{-12} cm^3 molecule^{-1} s^{-1} based on an average of six values selected from refs 22−36. There exists only one high-temperature value of the CF_3 recombination rate coefficient at $T = 1300$ K, which was obtained from a shock-wave experiment.[38] The reaction is still in the falloff region, and extrapolation to the high-pressure limit yields $k_\infty = 3.2 \times 10^{-11}$ cm^3 molecule^{-1} s^{-1}. Owing to the large variation of the room-temperature values and the uncertainty in the one high-temperature value, it is difficult to compare the CF_3 recombination reaction results from this study to experimental data.

(c) $CCl_3 + CCl_3$. The CCl_3 recombination reaction has been studied experimentally by several groups using indirect methods.[39−41] The first direct measurement was reported by Danis et al.[2] who observed the time-resolved decay of CCl_3 by UV absorption. They determined the recombination rate coefficients over a wide temperature range. They also performed RRKM calculations showing that the reaction was at the high-pressure limit under most of their experimental conditions. Only the highest value at 623 K exhibits a slight falloff behavior. Their data are, therefore, ideal for a comparison to the theoretical results from this work, and this is shown in Figure 8. The experimental results are in excellent agreement with those from this theoretical study, the calculated data at high temperatures having the same temperature dependence as the experimental data.

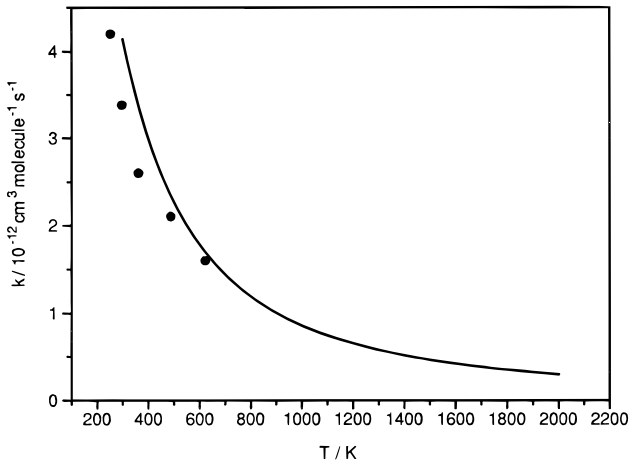

Figure 8. Comparison of the high-pressure limiting rate coefficient for the CCl_3 recombination versus temperature: (—) this work; (●) ref 2.

V. Conclusions

In this study CFTST was applied to the three recombination reactions (R1, R2, and R3) to determine the thermal rate coefficient at the high-pressure limit. It was shown that this approach, despite its approximations, yields satisfactory results, which are in good agreement with experimental data and other calculations. The relative ease of implementation and reduced computational effort, compared to the microcanonical FTST, makes CFTST ideal for reliable estimates of the magnitude and temperature dependence of high-pressure rate coefficients for barrierless association/dissociation reactions and for the prediction of trends in reaction rates within families of radical reactions.

The results of this study confirm the negative temperature dependence of the rate coefficients for the reactions R1, R2, and R3, which has already been observed in experimental investigations. For reaction R1, it should be noted that this experimental temperature dependence relies on extrapolations based on the master equation and is, therefore, subject to more uncertainty than a direct measurement. Nevertheless, similar results have been obtained in analyses by Hessler et al.[69] and Stewart et al.[70] This behavior can be attributed to the interaction between the $e^{-\beta V}$ radial potential term and the Γ hindrance function, which depends exclusively on the transitional mode potential V_{tr}. Since the TS moves to shorter interfragment separations (where V_{tr} is more repulsive), at higher temperatures Γ becomes smaller. Consequently, the rate coefficient decreases at higher temperatures. This effect becomes stronger for reactants with larger substituents. The rate coefficient decreases on going from CH_3 to CF_3 to CCl_3 recombination reaction, while the negative temperature dependence becomes steeper.

The potential-energy surface for the transitional modes was treated in an approximate manner by way of pairwise interactions between nonbonding atoms and a Morse interaction between the two bonding atoms, and the calculations were

designed primarily to investigate qualitatively the determinants of the temperature dependence. However, the use of parametrized ab initio potentials, such as that developed by Hirst et al.,[73] provides, in principle, a rigorous approach to the calculation of rate coefficients. The present analysis shows the strength of the CFTST approach, which is much less computationally demanding then the microcanonical (FTST) theory from which it is derived.

Acknowledgment. The assistance of Dr. M. A. Blitz and Kevin Resch (summer research assistant with D.M.W.) in determining the potential-energy surface parameters is deeply appreciated. Discussions with Drs. A. F. Wagner and J. P. Hessler are gratefully acknowledged. Financial support from the EC HCM and COPERNICUS programs (M.P. and S.H.R.), Zonta International (M.P.), the EPSRC Combustion Program (M.J.P.), and NSERC of Canada (D.M.W.) is also acknowledged.

References and Notes

(1) Roussel, P. B.; Lightfoot, P. D.; Caralp, F.; Catoire, V.; Lesclaux, R.; Forst, W. *J. Chem. Soc., Faraday Trans.* **1991**, *87*, 2367.

(2) Danis, F.; Caralp, F.; Veyret, B.; Loirat, H.; Lesclaux, R. *Int. J. Chem. Kinet.* **1989**, *21*, 715.

(3) Parkes, D. A.; Quinn, C. P. *Chem. Phys. Lett.* **1975**, *33*, 483.

(4) Wardlaw, D. M.; Marcus, R. A. *J. Phys. Chem.* **1986**, *90*, 5383.

(5) (a) Gorin, E. *Acta Physicochim. URSS* **1938**, *9*, 691. (b) Gilbert, R. G.; Pitt, I. G. *Research in Chemical Kinetics*; Compton, R. G., Hancock, G., Eds.; Elsevier Science New York, 1994; Vol. 2, p 147. (c) Pitt, I. G.; Gibert, R. G.; Ryan, K. R. *J. Phys. Chem.* **1995**, *99*, 239.

(6) Benson, S. W. *Can. J. Chem.* **1983**, *61*, 881.

(7) Quack, M.; Troe, J. *Ber. Bunsen-Ges. Phys. Chem.* **1974**, *78*, 240.

(8) (a) Wardlaw, D. M.; Marcus, R. A. *Chem. Phys. Lett.* **1984**, *110*, 230. (b) *J. Chem. Phys.* **1985**, *83*, 3462.

(9) (a) Garret, B. C.; Truhlar, D. G. *J. Chem. Phys.* **1979**, *70*, 1593. (b) Rai, S. N.; Truhlar, D. G. *J. Chem. Phys.* **1983**, *79*, 6064.

(10) Aubanel, E. E.; Wardlaw, D. M. *J. Phys. Chem.* **1989**, *93*, 3117.

(11) (a) Klippenstein, S. J.; Marcus, R. A. *J. Chem. Phys.* **1987**, *87*, 3410. (b) *J. Phys. Chem.* **1988**, *92*, 3105.

(12) (a) Klippenstein, S. J. *Chem. Phys. Lett.* **1990**, *170*, 71; *J. Chem. Phys.* **1991**, *94*, 6469; **1992**, *96*, 367. (b) Klippenstein, S. J. *J. Phys. Chem.* **1994**, *98*, 11459. (c) Klippenstein, S. J. *Chem. Phys. Lett.* **1993**, *214*, 418.

(13) (a) Smith, S. C. *J. Chem. Phys.* **1991**, *95*, 3404. (b) **1992**, *97*, 2406. (c) *J. Phys. Chem.* **1993**, *97*, 7034.

(14) Robertson, S. H.; Wagner, A. F.; Wardlaw, D. M. *J. Chem. Phys.* **1995**, *103* 2917.

(15) Macpherson, M. T.; Pilling, M. J.; Smith, M. J. C. *J. Phys. Chem.* **1985**, *89*, 2268.

(16) Slagle, I. R.; Gutman, D.; Davies, J. W.; Pilling, M. J. *J. Phys. Chem.* **1988**, *92*, 2455.

(17) Hwang, S. M.; Wagner, H. G.; Wolff, T. *Twenty-Third Symposium (International) on Combustion*; The Combustion Institute: Pittsburgh, PA, 1990; p 99.

(18) Walter, D.; Grotheer, H.-H.; Davies, J. W.; Pilling, M. J.; Wagner, A. F. *Twenty-Third Symposium (International) on Combustion*; The Combustion Institute: Pittsburgh, PA, 1990; p 107.

(19) Wagner, A. L.; Wardlaw, D. M. *J. Phys. Chem.* **1988**, *92*, 2462.

(20) Hippler, H.; Luther, K.; Ravishankara, A. R.; Troe, J. *Z. Phys. Chem.* **1984**, *142*, 1.

(21) Quack, M.; Troe, J. *Ber. Bunsen-Ges. Phys. Chem.* **1977**, *81*, 329.

(22) Ayscough, P. B. *J. Chem. Phys.* **1956**, *24*, 944.

(23) Ogawa, T.; Carlson, G. A.; Pimentel, G. C. *J. Phys. Chem.* **1970**, *74*, 2090.

(24) Basco, N.; Hathorn, F. G. M. *Chem. Phys. Lett.* **1971**, *8*, 291.

(25) Hiatt, R.; Benson, S. W. *Int. J. Chem. Kinet.* **1972**, *4*, 479.

(26) Skorobogatov, G. A.; Seleznev, V. G.; Slesar, O. N. *Dokl. Phys. Chem.* **1976**, *231*, 1292.

(27) Rossi, M.; Golden, D. M. *Int. J. Chem. Kinet.* **1979**, *11*, 775.

(28) Velichko, A. M.; Gordon, E. B.; Nedelkin, A. A.; Nikitin, A. I.; Tal′roze, V. L. *High Energy Chem.* **1985**, *19*, 58.

(29) Plumb, I. C.; Ryan, K. R. *Plasma Chem. Plasma Process.* **1986**, *6*, 205.

(30) Selamoglu, N.; Rossi, M. J.; Golden, D. M. *Chem. Phys. Lett.* **1986**, *124*, 68.

(31) Brown, C. E.; Orlando, J. J.; Reid, J.; Smith, D. R. *Chem. Phys. Lett.* **1987**, *142*, 213.

(32) Skorobogatov, G. A.; Dymov, B. P.; Lebedev, V. N.; Khripun, V. K. *Kinet. Catal.* **1987**, *28*, 682.

(33) Robertson, R. M.; Golden, D. M.; Rossi, M. J. *J. Phys. Chem.* **1988**, *92*, 5338.

(34) Skorobogatov, G. A.; Slesar, O. N.; Torbin, N. D. *Vestn. Leningr. Univ. Ser 4*: Fiz. Khim. **1988**, *4*, 30.

(35) Hidaka, Y.; Nakamura, T.; Kawano, H. *Chem. Phys. Lett.* **1989**, *154*, 573.

(36) Vakhtin, A. B. *Int. J. Chem. Kinet.* **1996**, *28*, 443.

(37) Hranisavljevic, J.; Michael, J. V. *J. Phys. Chem.*, in press.

(38) Glänzer, K.; Maier, M.; Troe, J. *J. Phys. Chem.* **1980**, *84*, 1681.

(39) Matheson, I. A.; Sidebottom, H. W.; Tedder, J. M. *Int. J. Chem. Kinet.* **1974**, *6*, 493.

(40) White, M. L.; Kuntz, R. R. *Int. J. Chem. Kinet.* **1973**, *5*, 187.

(41) Mare, G. R. De; Huybrechts, G. *Trans. Faraday Soc.* **1968**, *64*, 1311.

(42) Eidinoff, M. L.; Aston, J. G. *J. Chem. Phys.* **1935**, *3*, 379.

(43) Press, W. H.; Teukolsky, S. A.; Vetterling, W. T.; Flannery, B. P. *Numerical Recipes*; Cambridge University Press: Cambridge, 1992.

(44) Woost, B.; Bougeard, D. *J. Chem. Phys.* **1986**, *84*, 4810.

(45) Yamada, C.; Hirota, E.; Kawaguchi, K. *J. Chem. Phys.* **1981**, *75*, 5256.

(46) Dixon, D. A.; Van Catledge, F. A. *Int. J. Supercomput. Appl.* **1988**, *2*, 62 and references therein.

(47) Bozlee, B. J.; Nibbler, J. W. *J. Chem. Phys.* **1986**, *84*, 3798.

(48) Carlson, G. A.; Pimentel, G. C. *J. Chem. Phys.* **1966**, *44*, 4053.

(49) Yamada, C.; Hirota, E. *J. Chem. Phys.* **1983**, *78*, 1703.

(50) Snelson, A. *High Temp. Sci.* **1970**, *2*, 70.

(51) Andrews, L. *J. Chem. Phys.*, **1968**, *48*, 972.

(52) Horn, M.; Botschwina, P. *Chem. Phys. Lett.* **1994**, *228*, 259.

(53) Mayo, S. L.; Olafson, B. D.; Goddard, W. A. *J. Phys. Chem.* **1990**, *94*, 8897.

(54) Röthlisberger, U.; Laasonen, K.; Klein, M. L.; Sprik, M. *J. Chem. Phys.* **1996**, *104*, 3692 and references therein.

(55) Pedley, J. B. *Thermochemical Data and Structures of Organic Compounds*; Thermodynamics Research Centre, The Texas A&M University System: College Station, TX, 1994; Vol. 1.

(56) Kerr, J. A. *Strengths of Chemical Bonds in Handbook of Chemistry and Physics*, 77th ed.; Lide, D. R., Ed.; CRC Press: Boca Raton, FL, 1996.

(57) Atkinson, R.; Baulch, D. L.; Cox, R. A.; Hampson, R. F.; Kerr, J. A.; Rossi, M. J.; Troe, J. *J. Phys. Chem. Ref. Data* **1997**, *26*, 521, Evaluated kinetic, photochemical, and heterogeneous data for atmospheric chemistry: supplement V, IUPAC subcommittee on gas kinetic data evaluation for atmospheric chemistry.

(58) *JANAF Thermochemical Tables*, 2nd ed.; Stoll, D. R.; Prophet, H., Eds. ; NSRDS−NBS 37, 1971.

(59) Burcat, A.; McBride, B. *1997 Ideal Gas Thermodynamic Data for Combustion and Air-Pollution Use*; Technion Aerospace Engineering (TAE) Report; Technion Aerospace Engineering, Israel Institute of Technology: Haifa, Israel, 1997.

(60) Horn, H.; Oswald, M.; Oswald, R.; Botschwina, P. *Ber. Bunsen-Ges. Phys. Chem.* **1995**, *99*, 323 and references therein.

(61) Lide, D. *CRC Handbook of Chemistry and Physics*, 75th ed.; CRC Press: Boca Raton, FL, 1994; p 9.

(62) Hudgens, J. W.; Johnson, R. D.; Tsai, B. P.; Kafafi, S. A. *J. Am. Chem. Soc.* **1990**, *112*, 5763.

(63) Growcock, F. B.; Hase, W. L.; Simons, J. W. *Int. J. Chem. Kinet.* **1973**, *5*, 77.

(64) Marquardt D. W. *J. Soc. Ind. Appl. Math.* **1963**, *11*, 431.

(65) Bunker, P. R. *Molecular Symmetry and Spectroscopy*; Academic Press: New York, 1979.

(66) Troe, J. *Combust. Flame* **1989**, *78*, 59.

(67) Robertson, S. H.; Pilling, M. J.; Baulch, D. L.; Green, N. J. B. *J. Phys. Chem.* **1995**, *99*, 13452.

(68) Hessler, J. P. Private communication.

(69) (a) Du, H.; Hessler, J. P.; Ogren, P. J. *J. Phys. Chem.* **1996**, *100*, 974. (b) Hessler, J. P.; Ogren, P. J. *J. Phys. Chem.* **1996**, *100*, 984. (c) Hessler, J. P. *J. Phys. Chem.* **1996**, *100*, 2141.

(70) Stewart, P. H.; Larson, C. W.; Golden, D. M. *Combust. Flame* **1989**, *75*, 2570.

(71) Troe, J. *J. Phys. Chem.* **1979**, *83*, 114.

(72) Gilbert, R. G.; Luther, K.; Troe, J. *Ber. Bunsen-Ges. Phys. Chem.* **1983**, *87*, 169.

(73) Hirst, D. M.; Robertson, S. H.; Wardlaw, D. M. *J. Chem. Phys.* **1993**, *99*, 7748.